Shallow three-dimensional structure of the San Jacinto fault zone revealed from ambient noise imaging with a dense seismic array

Aurélien Mordret [1], Philippe Roux,[2] Pierre Boué[2] and Yehuda Ben-Zion[3]

[1]*Department of Earth, Atmospheric and Planetary Sciences, Massachusetts Institute of Technology (MIT), Cambridge, MA 02139, USA. E-mail:*
mordret@mit.edu
[2]*Institut des Sciences de la Terre (ISTerre), Universit Grenoble-Alpes (UGA), CNRS UMR 5275, Maison des Géosciences, 38400 Saint Martin dHères, France*
[3]*Department of Earth Sciences, University of Southern California (USC), Los Angeles, CA 90089 − 0740, USA*

SUMMARY

We use 1 month of continuous seismic waveforms from a very dense seismic network to image with unprecedented resolution the shallow damage structure of the San Jacinto fault zone across the Clark fault strand. After calculating noise correlations, high apparent velocity arrivals coming from below the array are removed using a frequency–wavenumber filter. This is followed by a double-beamforming analysis on multiple pairs of subarrays to extract phase and group velocity information across the study area. The phase and group velocity dispersion curves are regionalized into phase and group velocity maps at different frequencies, and these maps are inverted using a neighbourhood algorithm to build a 3-D shear wave velocity model around the Clark fault down to ∼500 m depth. The model reveals strong lateral variations across the fault strike with pronounced low-velocity zones corresponding to a local sedimentary basin and a fault zone trapping structure. The results complement previous earthquake- and seismic noise-based imaging of the fault zone at greater depth and clarify properties of structural features near the surface.

Key words: Seismic interferometry; Seismic tomography; Surface waves and free oscillations; Wave propagation; Wave scattering and diffraction.

1 INTRODUCTION

The properties and structures of the heavily damaged material in the top few hundred metres of the crust are understood only in general terms due to the lack of resolution of standard imaging techniques and strong local heterogeneities at shallow depths. Classic local earthquake tomography is best suited below 2–3 km, standard noise-based imaging with frequencies up to 1 Hz have resolution below 500 m, while small active seismic sources resolve mostly the first tens of metres of the subsurface. Having a better understanding of crustal structures and processes at this depth range is crucial, especially near fault zones, because of their great influence on observed seismic motion, crustal hydrology, reliability of underground facilities and numerous other applications. The low normal stress at shallow depth renders the subsurface material highly susceptible to failure and strongly attenuative, masking details of deeper structures and processes. Deriving detailed images of the very shallow crust can allow seismic velocity models to be developed essentially up to the surface, where they may be combined with information obtained from geological mapping and boreholes. The San Jacinto fault zone (SJFZ) is the most seismically active structure of the plate–boundary between the Pacific and North America plates in southern California, with a slip rate of about 10–15 mm yr^{-1} (e.g.

McGill *et al.* 2015; Rockwell *et al.* 2015). It runs parallel to the San Andreas fault to the NE and the Elsinore fault to the SW and is thought to have a recurrence rate of major earthquake ($M_W > 7.0$) of about 185–254 yr (Rockwell *et al.* 2015). The last earthquake which may have ruptured the total 230 km length of the fault likely occurred on 1800 November 22 (Rockwell *et al.* 2015), indicating that the SJFZ presents a serious seismic hazard for the region in the near future.

The Trifurcation area of the SJFZ, the region where the Clark fault is joined by the Bulk Ridge fault and the Coyote Creek fault (Fig. 1a), has ongoing small to moderate earthquake activity and generates >10 per cent of the recent seismicity in southern California (e.g. Ross *et al.* 2017). This complex faulting geometry is in contrast to the simpler section of the Clark fault to the NW, referred to as the Anza seismic gap (Sanders & Kanamori 1984), with a lack of microseismicity and potential source of M_W6.5 earthquakes. Previous imaging studies in the area used local earthquake tomography and ambient noise with frequencies up to 1 Hz to clarify properties of the fault zone at seismogenic depth (Scott *et al.* 1994; Allam & Ben-Zion 2012; Allam *et al.* 2014; Zigone *et al.* 2015). However, the properties in the top 500 m of the crust remained unresolved and are targeted in this work.
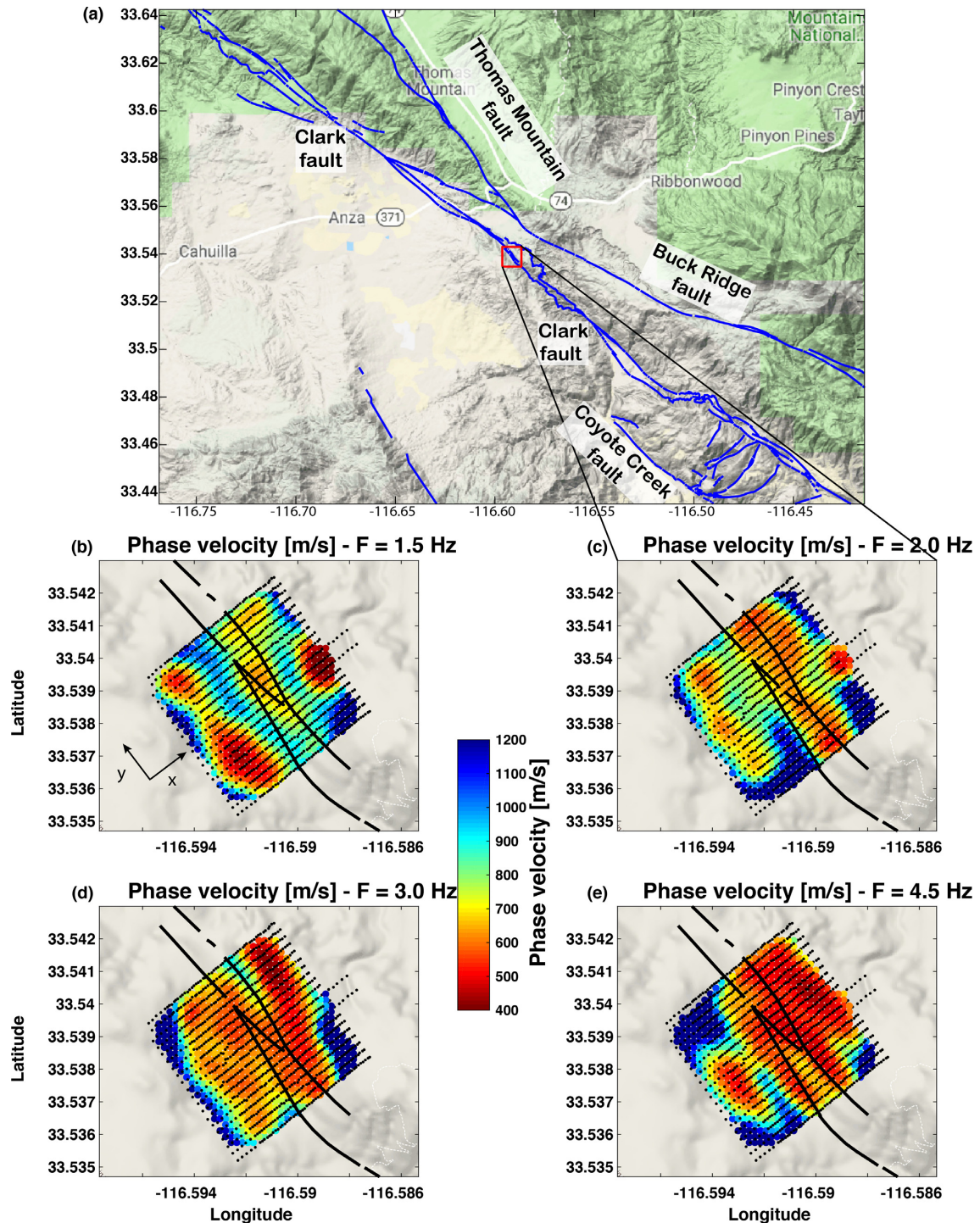
Figure 1. Phase velocity maps at four different frequencies obtained from DBF (Roux *et al.* 2016) on top of the local topography (Map data, Google, 2018). The black dots show the station configuration, the colour dots the local phase velocity. The thick black line indicates the surface trace of the Clark fault. The top panel (a) shows the general tectonic context of the studied area (red square) on a topography map of the Trifurcation area of the SJFZ (Map data, Google, 2018). The blue lines are the regional fault traces with their names. (b) 1.5 Hz, (c) 2.0 Hz, (d) 3.0 Hz and (e) 4.5 Hz.

Damage fault zone structures have strong heterogeneities of seismic properties including lateral interfaces that produce additional phases and complex wavefield (e.g. Ben-Zion & Aki 1990; Hillers *et al.* 2014). The intense seismicity and complex wavefield in the study area require using special techniques to suppress impulsive earthquake signals and extract Rayleigh surface waves from the remaining ambient seismic noise data that can be used for tomographic imaging (Shapiro *et al.* 2005; Roux 2009; Roux *et al.* 2011). This challenging task is accomplished using the pre-processing procedure and iterative double-beamforming (DBF) phase extraction technique of Roux *et al.* (2016). The obtained phase and group velocities of Rayleigh waves are inverted for shear wave velocities

in the shallow crust with a neighbourhood algorithm (Sambridge 1999). The derived 3-D shallow structure of the fault zone closes an important observational gap between previous seismic imaging studies and geological mapping in the area.

2 AMBIENT NOISE TOMOGRAPHY FROM A DENSE SEISMIC ARRAY

Following previous work on high-resolution imaging from ambient noise correlations of dense array data (e.g. Lin *et al.* 2013; Mordret *et al.* 2013a), we produce here local images of the shear wave velocity at the SJFZ. We first describe briefly the data and main methodological steps needed to construct accurate dispersion curves of Rayleigh waves from the noise correlations in the complex study area following Roux *et al.* (2016). The employed data were obtained by a dense rectangular array with 1108 (10 Hz) vertical geophones and linear dimensions of about 650 × 700 m^2 (Fig. 1). The array was centred on the damage structure of the Clark fault in the Trifurcation area of the SJFZ, southeast of Anza (Fig. 1), and recorded waveforms continuously at 500 Hz for about 1 month in 2014 (Ben-Zion *et al.* 2015). Each row along the fault-normal (*x*) direction had 55 sensors with an intersensor distance of 10 m, and the nominal separation between the rows in the along-strike (*y*) direction was 30 m. Each element of the seismic array provided continuous GPS-synchronized records.

2.1 Reliable extraction of Rayleigh waves information in fault zone region

Despite the incoherent noise generated by the ocean and by nearby sources (e.g. wind or human related), recent analyses suggested that numerous impulsive signals recorded by the array are generated by sources below the surface (Ben-Zion *et al.* 2015). Their apparent random temporal occurrence, without clear diurnal pattern, suggests that they do not have a thermal or man-made origin. In addition to many distinguishable microseismic events (Meng & Ben-Zion 2018), the waveforms contain large sets of long bursts that are typically grouped with the ambient seismic noise extending down to 1 Hz. To account for the presence of impulsive spikes in the waveforms, one-bit noise correlation is applied to 1 d long recording windows between all sensor pairs of the network. The averaged 1 d cross-correlations show a strong contribution around time $t = 0$, which suggests that most of the coherent signals are coming from below the array with very high apparent velocities, consistent with the presence of body waves (Roux *et al.* 2016). Because of the complexity of the ambient wavefield, all the processing (from raw data to velocity measurements) is done in narrow frequency band (about an octave). This increases significantly the quality of the measurement (for instance, one-bit normalization becomes quite robust) as well as the computational effort.

After getting the noise correlations, surface waves can be separated from body waves using a frequency–wavenumber filtering to remove phase velocities greater than 1000 m s^{-1} at each frequency. Despite unfavourable noise–source distribution for surface waves, both phase and group velocity maps are obtained at 13 discrete frequencies from 1.3 to 5 Hz. This is done using a DBF algorithm applied to a set of ∼400 000 subarray pairs, each made of 25 neighbouring sensors selected among the dense seismic array (Roux *et al.* 2016). Similar to standard beamforming where time-delayed traces from one source are stacked across an array of receivers to find the speed and direction of the incoming waves, the DBF stacks time-delayed traces from multiple (virtual) sources on a pair of (virtual) source–receiver arrays. Using cross-correlations C_{ij} between each pair of sensors within the two subarrays, the time-dependent DBF can be expressed as (Roux *et al.* 2016)

$$\text{DBF}(t) = \sum_{i,j} C_{ij}(t - \delta_{ij}), \tag{1}$$

where δ_{ij} is the time delay between each station *i* and *j* among the two arrays. The elevation difference at each sensor is taken into account in the time-delay computation. The DBF analysis is essential here to separate the fundamental Rayleigh wave from higher order modes and other spurious arrivals that are superimposed at short distances in the above-mentioned frequency bands. Despite the fact that higher modes can be used to better constrain velocity models in surface wave tomography (Tomar *et al.* 2018), their identification is often difficult and hence less robust (Boué *et al.* 2016). Here, we are seeking a good identification of the fundamental mode by increasing its signal-to-noise ratio (Boué *et al.* 2014). The DBF provides both the slowness and traveltime of each extracted wavelet, which can be used to derive phase and group velocity information at each frequency when accumulated over all possible subarray pairs.

Figs 1 and 2 show Rayleigh wave phase and group velocity maps obtained at 1.5, 2, 3 and 4 Hz from the phase slowness and traveltime inversion on a regular horizontal grid with steps of 15 m. The tomography inversion starts from a homogeneous initial model, assuming straight rays as propagation paths and an *a priori* error covariance matrix that decreases exponentially with distances over 50 m (Roux *et al.* 2016). For the group velocity map, the inversion is performed with a random subsample of all the measurements and repeated 1000 times. The average results of these 1000 inversions give the final group velocity maps and the standard deviation gives their uncertainties. We use this procedure to reduce the computational burden of inverting more than 400 000 dispersion curves at once. This also allows us to obtain robust statistical estimate of the group velocity uncertainties. At each frequency, the phase or group velocity inversions produce a residual variance reduction of ∼95 per cent relative to the phase slowness and ∼98 per cent relative to the traveltimes of the homogeneous model. The topography has a maximum of 50 m elevation difference on the array and is not taken into account in the inversions (as suggested in Pilz *et al.* 2013). The smallest wavelength that we are measuring is on the order of 60–65 m and may only affect our estimation of the group velocity for which the distance between the subarrays is used to compute the velocity. Despite this approximation, the correlation between the group velocity maps and the topography is not obvious.

Note that with this approach phase velocity is assumed to accumulate over propagation distance, similarly to group velocity, following the Fermat principle. However, phase velocity should instead be considered as a local value below each 25-element array used to perform the DBF. This requires extracting two phase slowness instead of one following the procedure described in Roux *et al.* (2016; see their eqs 2– 4 for details) at the price of a significantly larger computation effort. This assumption is valid if the propagation medium is not too complex, that is, when the two subarrays are close to each other. At longer distance, multipathing is stronger and the phase velocity estimations are less reliable. As for eikonal tomography (Lin *et al.* 2009; Mordret *et al.* 2013c), the phase slowness extracted from each subarray pair through DBF can be locally averaged to produce equivalent phase velocity maps (Fig. 1) and used to estimate the uncertainties.
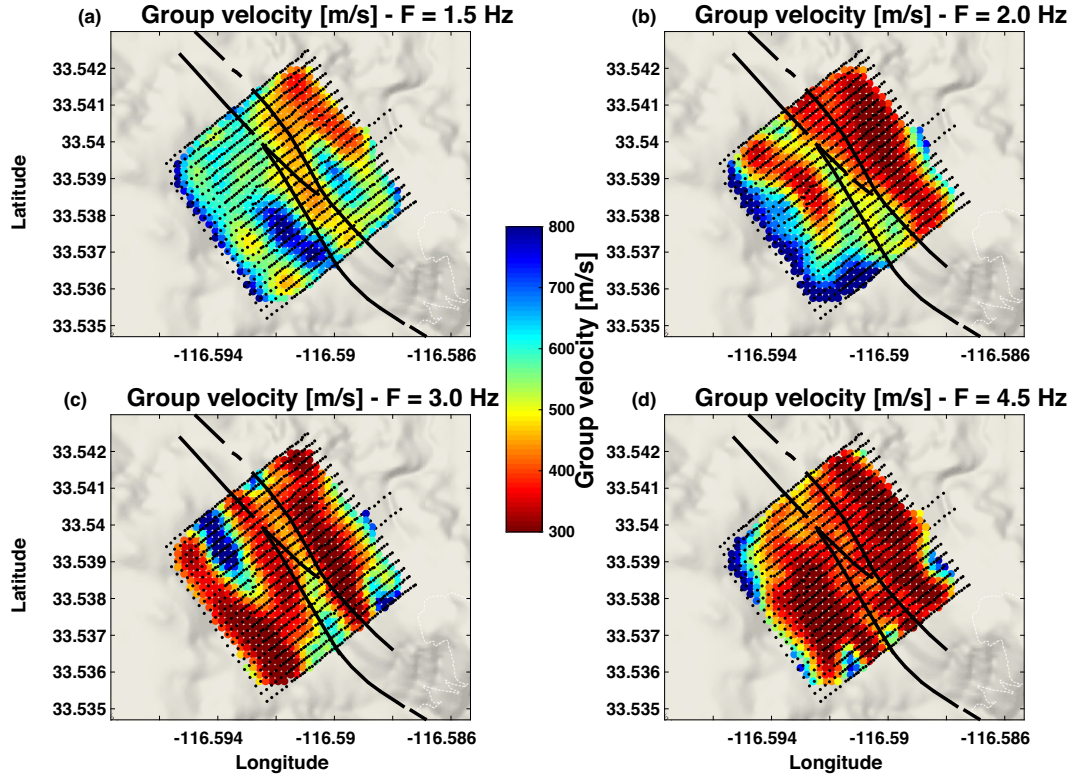
Figure 2. Group velocity maps at four different frequencies obtained from DBF (Roux *et al.* 2016) on top of the local topography (Map data, Google, 2018). The black dots show the station configuration, the colour dots the local group velocity. The thick black line indicates the surface trace of the fault. (a) 1.5 Hz, (b) 2.0 Hz, (c) 3.0 Hz and (d) 4.5 Hz.

The tomography results show strong lateral variations across the fault traces. The red low-velocity zone near the right fault line observed at lower frequencies in the phase velocity maps (Figs 1 a and b) corresponds to the fault zone trapping structure identified in Ben-Zion *et al.* (2015) and Qin *et al.* (2018) using active experiment data and earthquake waveforms. The results for increasing frequencies have complex features that correspond progressively to shallower depth. Note that phase velocity maps seem to be at first sight more interpretable than group velocity maps as suggested from their relative sensitivity kernel analysis (Supporting Information Fig. S1). Phase velocity sensitivity always exhibits a positive kernel with one main maximum implying that a shear wave velocity anomaly at depth will be positively correlated with the phase velocity at the frequency sensitive to this depth. On the other hand, group velocity kernels exhibit two main extrema: one positive and one negative at different depths. Therefore, at a single frequency, group velocity maps show the weighted average of shear velocity structures that are positively correlated at one depth with shear velocity structures that are negatively correlated at another depth. This makes it difficult to interpret the resulting group velocity values. Another consequence of the group velocity kernel shape is that a single positive shear wave velocity anomaly at a specific depth may be seen as positive or negative group velocity anomalies depending on frequency. The wavelength range of the Rayleigh waves used here suggests that the imaging results characterize the top 50 m to 400–500 m of the crust.

2.2 Inversion with a neighbourhood algorithm

The full set of phase and group velocity maps provides local dispersion curves at each cell of the map. These local dispersion curves

for phase and group velocities are jointly inverted to obtain local 1-D profiles of V_s versus depth. The ensemble of every best local 1-D model constitutes the final 3-D V_s model.

We use a Monte-Carlo approach to invert the dispersion curves at depth because of the strong nonlinearity of the problem and the absence of accurate *a priori* starting velocity model. This Monte-Carlo approach is based on a neighbourhood algorithm (Sambridge 1999) and is described in detail by Mordret *et al.* (2014). This algorithm has the advantage of exploring entirely the model space using a Voronoï cell discretization and increasing the focus on its most promising areas as the iteration number increases. The general 1-D velocity profile is parametrized by a power-law backbone, suitable for modelling compacting sediments (e.g. Wathelet *et al.* 2004), modified by two cubic-spline anomalies. The bottom layer of the model is a half-space. The model is described by the following equation:

$$V_s(d) = V_0 \left[(d+1)^\alpha - (d_0 + 1)^\alpha + 1 \right] + \sum_{n=1}^{2} A_n S_n^\beta(d), \qquad (2)$$

where V_s is the shear wave velocity, d is the depth, V_0 is the velocity at depth $d_0 = 10$ m, α is the curvature of the power law, S_n are the spline basis functions, β is a parameter describing the depth distribution of the splines (Mordret *et al.* 2015) and A_n are the amplitudes of the splines. The local 1-D models are discretized using 19 homogeneous layers with logarithmic increasing thickness between the surface and depth d_n. During the inversion, the P-wave velocity is scaled to V_s using a V_p/V_s ratio that varies linearly between V_p/V_{s_0} at the surface and V_p/V_{s_n} at the depth d_n to take into account the sensitivity of Rayleigh waves to V_p in the near surface (Supporting Information Fig. S1). Below d_n, the V_p/V_s ratio is set

Table 1. Inverted parameters and their ranges.

Parameter	Unit	Min	Max
V_0	m s^{-1}	100	600
α		0.15	0.3
β		2	5
A_1	m s^{-1}	-500	1000
A_2	m s^{-1}	-500	1000
d_n	m	400	1000
V_p/V_{s_0}		1.5	2.5
V_p/V_{s_n}		1.6	2.0

to 1.73. The density is scaled to V_p using the empirical relationship of Brocher (2005). The depth inversion searches for the optimum parameters V_0, α, β, A_1, A_2, V_p/V_{s_0}, V_p/V_{s_n} and the depth d_n of the half-space at each point of the geographical grid. The ranges explored by the algorithm for the eight parameters are shown in Table 1.

We sample a total of 24 000 models at each geographical point of our grid. The initial random sampling is done with 10 001 models; then the Voronoï cells around the best 1000 models are resampled with 2 models and this process is iterated seven times (Mordret *et al.* 2014). The final model is the average of the 2000 best models (with the lowest misfits). The uncertainties of the velocity model are estimated by the standard deviation of the posterior distribution of the best 2000 models. Figs 3(a) and (b) show two examples of local inversions at two different positions on the grid (Fig. 3c). The colours show the misfit, the grey curves are the best model and its associated dispersion curves, and the black bars are the measured dispersion curves. During each inversion, we used a misfit defined by Mordret *et al.* (2014) as a ratio of two surface areas, Misfit $= \mathrm{d}S/S$, with S being the integral surface area of the measured dispersion curve and its error bars and dS the integral surface area of the synthetic dispersion curve outside of S. With this definition, the misfit presents a wider minimum area and permits to retain dispersion curves as long as they fit the data within their error bars.

The misfit map has strong lateral variations (Fig. 3c) that mostly reflect difficulties to fit some local phase dispersion curves (Fig. 3a). For some frequencies, the phase velocity has large uncertainties and does not seem to be consistent with velocities at neighbouring frequencies. This might indicate discontinuities within cell's phase dispersion curves due to lateral heterogeneities, contamination by higher order modes, body waves or local anthropogenic noise (southwest of the fault). Local measurements of phase velocities across the fault reveal strong changes on short distances associated with low-velocity damaged zones (see fig. 12 in Roux *et al.* 2016). Future work will focus on local extraction of phase slowness as discussed in Section 2.1 and its interpretation through both local anisotropy and damage.

The group velocities are comparatively more robust, essentially because of the lack of phase ambiguity measurements but they also exhibit discontinuities to some extent. Again, contamination by higher modes, body waves or sensor coupling may be at the origin of these jumps. To assess the benefit of jointly inverting phase velocities with group velocities, we performed an inversion of the group velocity alone (Supporting Information Fig. S2). For the same two points as in Fig. 3 we achieve much smaller misfits. However, it clearly appears that the dispersion curves are overfitted and do not correspond to physically and geologically reasonable velocity models. The addition of phase velocity dispersion curves in the inversion, despite their larger uncertainties, helps to diminish the non-uniqueness of the solution (e.g. Shapiro & Ritzwoller 2002). In

conclusion, the constraints brought by the phase velocities, although weak, facilitate the rejection of highly unreasonable models and strengthen the robustness of the results.

3 INVERSION RESULTS

The derived 3-D model shows lateral velocity variations of about 20–30 per cent at all depths (Figs 4a, b and 5a, b) with several structures parallel to the fault strike (Figs 4 a and b). The velocity uncertainties are correlated with the velocity structures with higher uncertainties for higher velocities (Figs 4 c and d). They also tend to increase with depth, showing uncertainties smaller than 100 m s^{-1} above 100 m depth and up to 250–300 m s^{-1} below this depth. This reflects the extra constraint from V_p and density in the near surface (Supporting Information Fig. S1). The inversion results confirm that the assumed initial average velocity profile following a modified power law is a good model for the very shallow velocity structure (Fig. 5c). The two surface fault traces (black dashed lines in Figs 5 a and b) clearly delineates a low-velocity zone encompassed by higher velocities to the SW and slightly lower velocities to the NE (Fig. 6). This sharp lateral contrast even more clearly present in the depth variations of the isovelocity contour at $V_s = 850$ m s^{-1} (Fig. 7), which is a proxy for the transition between the loose near surface sediments and the more compact rocks at depth. A trough beneath the surface fault traces is consistent with damaged rocks producing deeper low-velocity material than directly to the west. This low-velocity zone corresponds to the local seismic trapping structure observed by Ben-Zion *et al.* (2015) and Qin *et al.* (2018).

Given the final misfit in the most southwestern part of the model (Fig. 3c) and the large uncertainties associated with the estimations of the depth of the half-space (Fig. 3a), the deep trough in the SW of Fig. 7, at the location of a small sedimentary basin, should be interpreted with caution. Overall, the robust qualitative features of the model (and the ones explaining most of the variance in the data) are the power-law increase of the velocity with depth within the near surface sediments, consistent with compaction (e.g. Baldwin & Butler 1985; Bachrach *et al.* 2000), the lateral variations across the fault traces and the depth variations of the base of the compacting layer. In such a complex environment, however, this simple model might be quantitatively biased by the simplifications we make during the modelling. Assuming a linear gradient-like V_p/V_s ratio in the near surface is one of them. Supporting Information Fig. S3 shows horizontal and vertical slices through the 3-D V_p/V_s model. We can observe lateral variations that seem to be parallel to the fault strike and most of the model exhibit an increase of V_p/V_s ratio with depth. The scattering of the best models in Fig. 3 suggests that this increase may not be a robust feature of our inversion. Among other simplifications, we do not take into account the attenuation and the anisotropy while inverting for the velocity model. These parameters may not be negligible in the centre and heavily damaged part of this fault zone as highlighted by previous studies (Ben-Zion *et al.* 2015; Hillers *et al.* 2016). However, the pre- and post-processing used to compute the noise correlations and extract the Rayleigh waves strongly affect the signal amplitudes, making the extraction of attenuation information difficult. Analysing the noise data with a procedure of the type developed by Liu *et al.* (2015) can provide information on the attenuation coefficients. Regarding anisotropy the vertical component sensors are used in this study can provide information only on the azimuthal anisotropy of the Rayleigh waves. Resolving radial anisotropy (e.g. Tomar *et al.* 2016) expressing the difference in propagation speed between horizontally
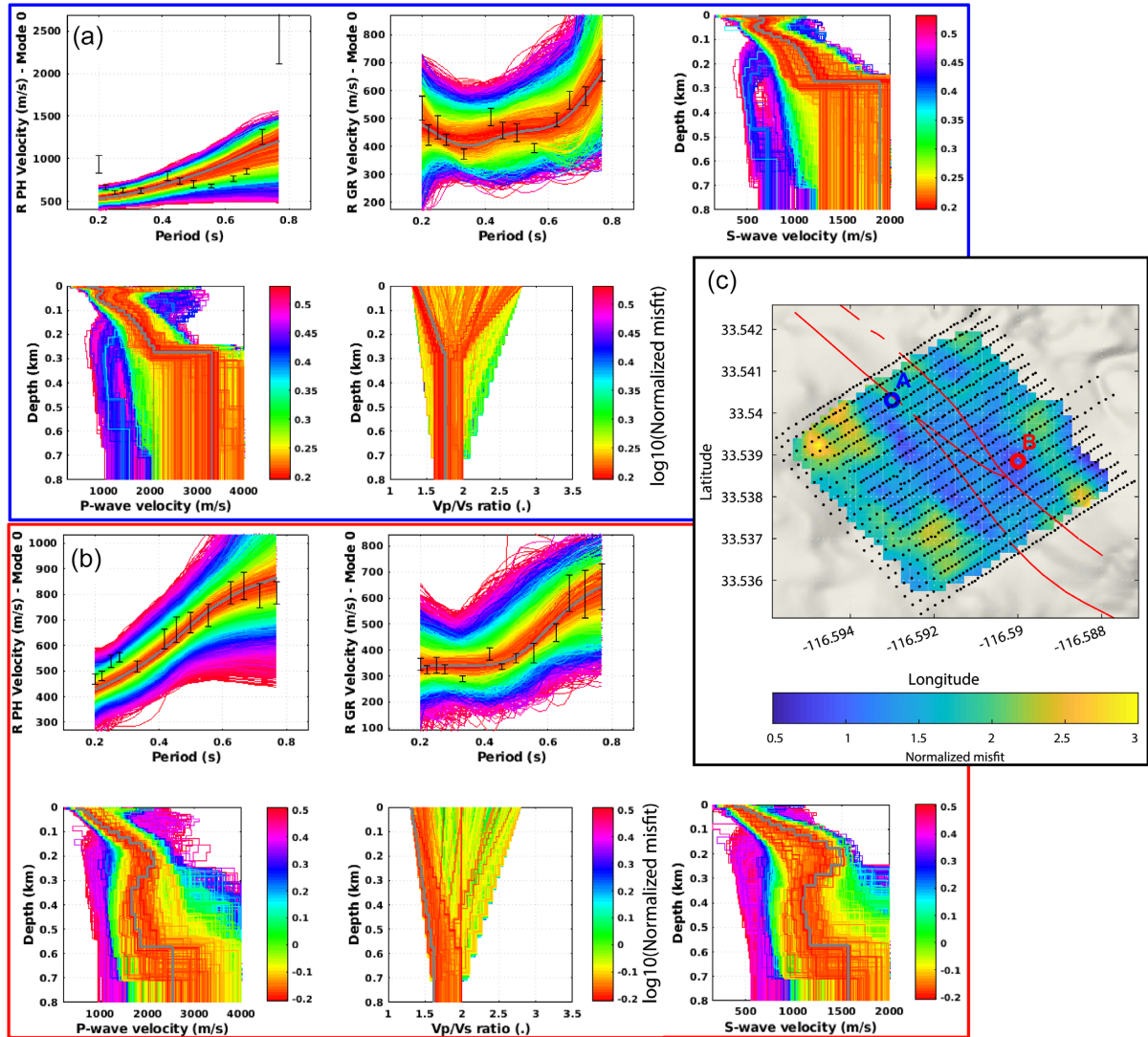
Figure 3. Local depth inversion at two locations in the model: the top-left panel shows the phase velocity dispersion curve fit, the top-middle panel shows the group velocity dispersion curve fit and the top-right (bottom right for point B) panel shows the sampled V_s models. The bottom-left panel shows the sampled V_p models and the bottom-middle panel the V_p/V_s ratios. The inverted data are in black with the error bars; the best model and the dispersion curves associated with the best model are in grey. The colour of the modelled dispersion curves and their associated models indicate their misfit value. (a) Inversion of a point on top of the main Clark fault trace. (b) Inversion of a point east of the fault. (c) Map of the best model misfit on top of the local topography (Map data, Google, 2018). The fault traces are shown by the red lines. The seismic array is shown by the black dots and the locations of the points inverted in panels (a) and (b) are indicated by the blue and red circles, respectively.

and vertically polarized waves requires three-component data. An analysis of azimuthal anisotropy through an eikonal tomography approach (Mordret *et al.* 2013b; Zigone *et al.* 2015) will be the subject of future work.

4 DISCUSSION AND CONCLUSIONS

Building on the methodological work of Roux *et al.* (2016), we image with an unprecedented resolution the shallow damage structure of the SJFZ at the site of the dense seismic deployment (Fig. 1). The complex environment, both in terms of structure and variety of seismic signals, requires the use of innovative techniques to extract the surface wave information needed to perform the tomography. The derived 3-D shear wave velocity model for the top 500 m of the crust complements information obtained with more standard earthquake- and noise-based imaging techniques on the deeper structure of the

fault zone, and allows direct comparisons with geological observations made at the surface (Wade *et al.* 2017).

A previous attempt to image fault zone structure with ocean-induced seismic noise was performed on the San Andreas fault in Parkfield at lower frequency (<0.35 Hz) and at a larger scale from 30 stations in a 10 km x 10 km area (Roux *et al.* 2011). A 1.3 km wide steep dipping was imaged from less than 400 local dispersion curves for Love waves. Joint inversion of body wave arrival times and these surface wave dispersion curves were applied to further constrain a "U-shaped" feature of the 3-D seismic structure around San Andreas Fault Observatory at Depth. (SAFOD) (Zhang *et al.* 2014). It seems that a similar feature is observed in Fig. 7, though at a much smaller scale. In our study area the U-shaped feature is produced by a narrow low-velocity zone delimited by the surface fault traces trapped between two higher velocity ridges to the SW and the NE(Figs 6–7). Qin *et al.* (2018) concluded based on earthquake
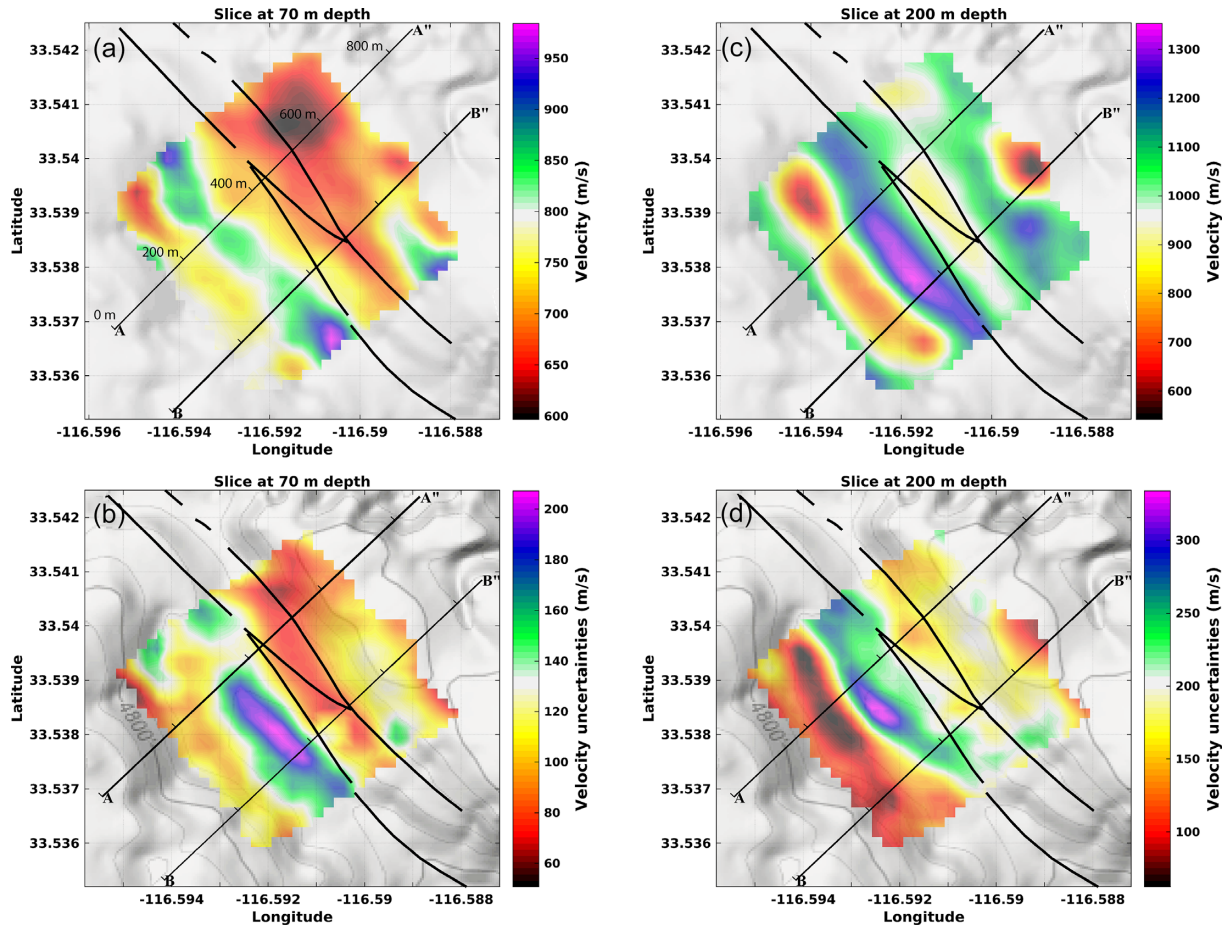
Figure 4. Horizontal slices in the 3-D velocity model at 70 m depth (a) and 200 m depth (b) on top of the local topography (Map data, Google, 2018). Horizontal slices in the 3-D uncertainty model at 70 m depth (a) and 200 m depth (b) on top of the local topography. The main Clark fault trace is shown with thick black curves. The locations of the vertical profiles shown in Fig. 5 are displayed with the thin black lines and graduated every 200 m.
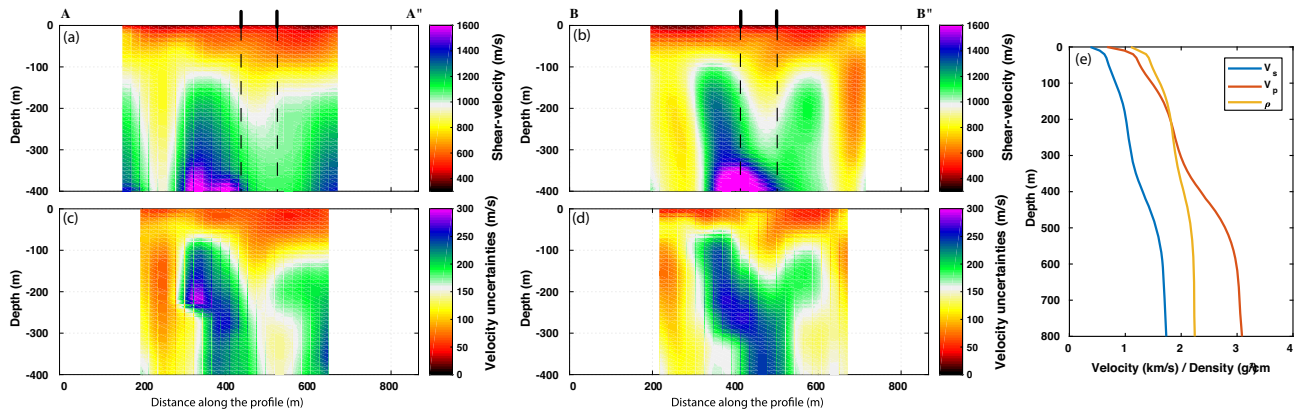

Figure 5. Vertical slices in the 3-D velocity model, the bold black lines and the dashed lines show the surface traces of the faults and their vertical prolongation at depth, respectively. (a) Profile A–A", (b) Profile B–B". Vertical slices in the 3-D uncertainty model. (c) Profile A–A", (d) Profile B–B". The locations of the profiles are shown in Fig. 4. (e) Average V_p, V_s and density models.

waveforms that the SW fault trace represents the main seismogenic fault separating two different crustal blocks at depth. The asymmetry between the high velocities to the SW and the lower velocities to the NE tends to confirm this interpretation. Theoretical and numerical results indicate that earthquakes on a bimaterial interface tend to have preferred rupture direction (Ben-Zion 2001, and references therein) and produce asymmetric shallow damage structure on the

less compliant side of the fault at depth (e.g. Ben-Zion & Shi 2005; Xu & Ben-Zion 2017). In the study area, regional tomographic images have shown that the NE side of the main Clark fault is faster than the SW block at seismogenic depth (Scott *et al.* 1994; Allam & Ben-Zion 2012; Allam *et al.* 2014; Zigone *et al.* 2015). Therefore, it is expected that rock damage be more pronounced on the NE side of the fault in the near surface, generating a shallow velocity contrast
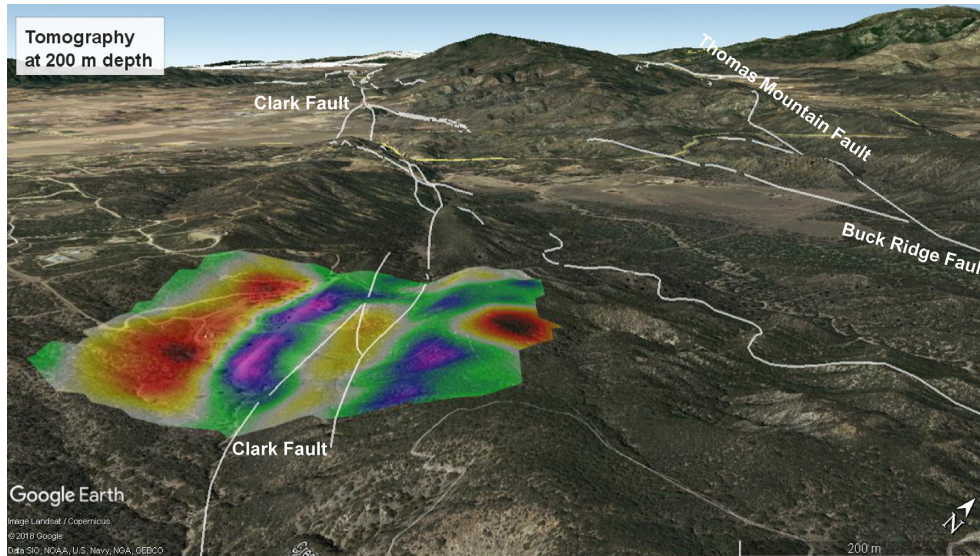
Figure 6. The velocity model in the tectonic context: shear wave velocity model at 200 m depth draped on the local topography. The fault traces are shown with white lines. The orange/red areas indicate slower than average velocity zones. The green/blue areas indicate faster than average velocity zones.
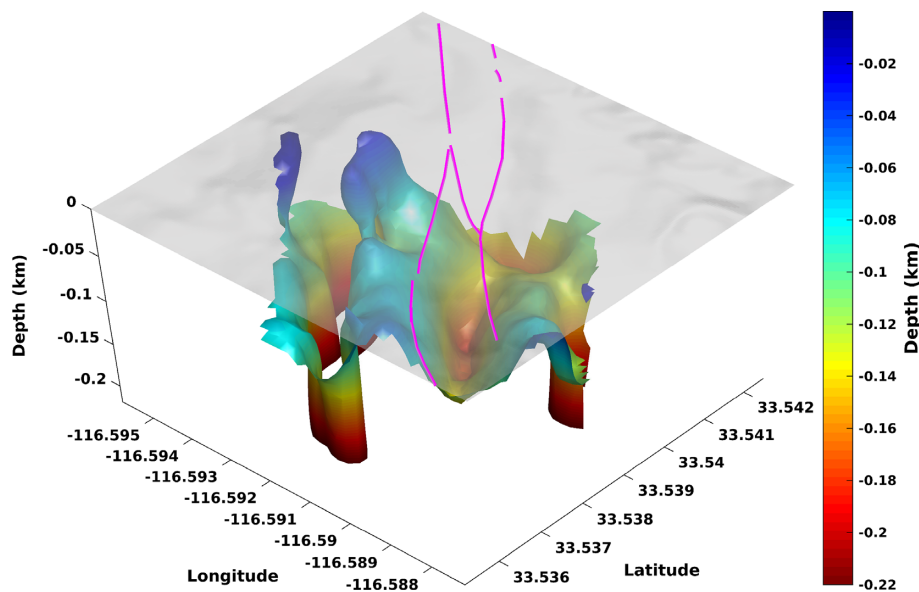

Figure 7. Isovelocity contour at $V_s = 850$ m s^{-1} showing the base of the compacting sediments. The fault trace is underlain by a trough of low-velocity material restricted by ridges of higher velocity material in the southwest and northeast. The fault trace is shown with the magenta lines at the surface on top of shaded digital elevation model. The isovelocity surface and the digital elevation model do not have the same vertical exaggeration.

inversion between the local scale and the regional scale structures. This is confirmed by the local contrast of seismic velocities across the main Clark fault imaged in this study (Figs 4 and 6) and is consistent with local geological mapping (Wade *et al.* 2017) and agrees with the general NW directivity of earthquake ruptures in the area.

The results of this work mainly provide isotropic shear wave velocities of the subsurface structure. Future studies can improve the seismological characterization of the study area by deriving information on the compressional wave velocity, attenuation coefficients and anisotropy. Research on some of these topics is currently under way. Fang *et al.* (2016) derived a 3-D velocity model for the plate–boundary region around the SJFZ with a nominal resolution of about 3 km from joint inversion of surface wave and body wave measurements. Similar analysis can be performed for the site of the dense deployment using our surface wave results and the collection

of active shots recorded on the dense seismic grid (Ben-Zion *et al.* 2015). Following Nakata *et al.* (2015), refracted and/or reflected body wave arrivals could also be extracted directly from ambient noise correlations from the microseismic activity at depth in the fault zone. The lateral spatial resolution in the sampled area should be lower than 50 m for a detailed 3-D image down to 500 m at depth.

The site of the dense deployment used in this work is becoming a natural laboratory for collecting and correlating different types of geological data (detailed mapping, laboratory characterization of rock samples) and geophysical results (seismic, geodetic, electrical resistivity, GPR). The 3-D velocity model developed in this paper for the very shallow crust provides a fundamental component for the effort to compare and correlate different fault zone data sets. It will also help to better constrain results on temporal changes of

seismic velocities from various sources, and understand properties of earthquake ruptures in the area.

REFERENCES

Allam, A. & Ben-Zion, Y., 2012. Seismic velocity structures in the southern California plate–boundary environment from double-difference tomography, *Geophys. J. Int.,* **190**(2), 1181–1196.

Allam, A., Ben-Zion, Y., Kurzon, I. & Vernon, F., 2014. Seismic velocity structure in the Hot Springs and Trifurcation areas of the San Jacinto fault zone, California, from double-difference tomography, *Geophys. J. Int.,* **198**(2), 978–999.

Bachrach, R., Dvorkin, J. & Nur, A.M., 2000. Seismic velocities and Poisson's ratio of shallow unconsolidated sands, *Geophysics,* **65**(2), 559–564.

Baldwin, B. & Butler, C.O., 1985. Compaction curves, *AAPG Bull.,* **69**(4), 622–626.

Ben-Zion, Y., 2001. Dynamic ruptures in recent models of earthquake faults, *J. Mech. Phys. Solids,* **49**(9), 2209–2244.

Ben-Zion, Y. & Aki, K., 1990. Seismic radiation from an *SH* line source in a laterally heterogeneous planar fault zone, *Bull. Seism. Soc. Am.,* **80**(4), 971–994.

Ben-Zion, Y. & Shi, Z., 2005. Dynamic rupture on a material interface with spontaneous generation of plastic strain in the bulk, *Earth Planet. Sci. Lett.,* **236**(1–2), 486–496.

Ben-Zion, Y. *et al.*, 2015. Basic data features and results from a spatially dense seismic array on the San Jacinto fault zone, *Geophys. J. Int.,* **202**(1), 370–380.

Boué, P., Roux, P., Campillo, M. & Briand, X., 2014. Phase velocity tomography of surface waves using ambient noise cross correlation and array processing, *J. Geophys. Res.,* **119**(1), 519–529.

Boué, P., Denolle, M., Hirata, N., Nakagawa, S. & Beroza, G.C., 2016. Beyond basin resonance: characterizing wave propagation using a dense array and the ambient seismic field, *Geophys. J. Int.,* **206**(2), 1261–1272.

Brocher, T.M., 2005. Empirical relations between elastic wavespeeds and density in the Earth's crust, *Bull. Seism. Soc. Am.,* **95**(6), 2081–2092.

Fang, H., Zhang, H., Yao, H., Allam, A., Zigone, D., Ben-Zion, Y., Thurber, C. & van der Hilst, R.D., 2016. A new algorithm for three-dimensional joint inversion of body wave and surface wave data and its application to the Southern California plate boundary region, *J. Geophys. Res.,* **121**(5), 3557–3569.

Hillers, G., Campillo, M., Ben-Zion, Y. & Roux, P., 2014. Seismic fault zone trapped noise, *J. Geophys. Res.,* **119**(7), 5786–5799.

Hillers, G., Roux, P., Campillo, M. & Ben-Zion, Y., 2016. Focal spot imaging based on zero lag cross-correlation amplitude fields: application to dense array data at the San Jacinto fault zone, *J. Geophys. Res.,* **121**(11), 8048–8067.

Lin, F.-C., Ritzwoller, M.H. & Snieder, R., 2009. Eikonal tomography: surface wave tomography by phase front tracking across a regional broadband seismic array, *Geophys. J. Int.,* **177**(3), 1091–1110.

Lin, F.-C., Li, D., Clayton, R.W. & Hollis, D., 2013. High-resolution 3D shallow crustal structure in Long Beach, California: application of ambient noise tomography on a dense seismic array, *Geophysics,* **78**(4), Q45–Q56.

Liu, X., Ben-Zion, Y. & Zigone, D., 2015. Extracting seismic attenuation coefficients from cross-correlations of ambient noise at linear triplets of stations, *Geophys. J. Int.,* **203**(2), 1149–1163.

McGill, S.F., Spinler, J.C., McGill, J.D., Bennett, R.A., Floyd, M.A., Fryxell, J.E. & Funning, G.J., 2015. Kinematic modeling of fault slip rates using new geodetic velocities from a transect across the Pacific-North America plate boundary through the San Bernardino Mountains, California, *J. Geophys. Res.,* **120**(4), 2772–2793.

Meng, H. & Ben-Zion, Y., 2018. Detection of small earthquakes with dense array data: example from the San Jacinto fault zone, southern California, *Geophys. J. Int.,* **212**(1), 442–457.

Mordret, A., Landès, M., Shapiro, N., Singh, S., Roux, P. & Barkved, O., 2013a. Near-surface study at the Valhall oil field from ambient noise surface wave tomography, *Geophys. J. Int.,* **193**(3), 1627–1643.

Mordret, A., Shapiro, N.M., Singh, S., Roux, P., Montagner, J.-P. & Barkved, O., 2013b. Azimuthal anisotropy at Valhall: the Helmholtz equation approach, *Geophys. Res. Lett.,* **40**(11), 2636–2641.

Mordret, A., Shapiro, N.M., Singh, S.S., Roux, P. & Barkved, O.I., 2013c. Helmholtz tomography of ambient noise surface wave data to estimate Scholte wave phase velocity at Valhall Life of the Field, *Geophysics,* **78**(2), WA99–WA109.

Mordret, A., Landès, M., Shapiro, N., Singh, S. & Roux, P., 2014. Ambient noise surface wave tomography to determine the shallow shear velocity structure at Valhall: depth inversion with a Neighbourhood Algorithm, *Geophys. J. Int.,* **198**(3), 1514–1525.

Mordret, A., Rivet, D., Landès, M. & Shapiro, N.M., 2015. Three-dimensional shear velocity anisotropic model of Piton de la Fournaise Volcano (La Réunion Island) from ambient seismic noise, *J. Geophys. Res.,* **120**(1), 406–427.

Nakata, N., Chang, J.P., Lawrence, J.F. & Boué, P., 2015. Body wave extraction and tomography at Long Beach, California, with ambient-noise interferometry, *J. Geophys. Res.,* **120**(2), 1159–1173.

Pilz, M., Parolai, S. & Bindi, D., 2013. Three-dimensional passive imaging of complex seismic fault systems: evidence of surface traces of the Issyk–Ata fault (Kyrgyzstan), *Geophys. J. Int.,* **194**(3), 1955–1965.

Qin, L., Ben-Zion, Y., Qiu, H., Share, P., Ross, Z. & Vernon, F., 2018. Internal structure of the San Jacinto fault zone in the trifurcation area southeast of Anza, California, from data of dense seismic arrays, *Geophys. J. Int.,* **213**(1), 98–114.

Rockwell, T.K., Dawson, T.E., Ben-Horin, J.Y. & Seitz, G., 2015. A 21-event, 4,000-year history of surface ruptures in the Anza seismic gap, San Jacinto fault, and implications for long-term earthquake production on a major plate boundary fault, *Pure Appl. Geophys.,* **172**(5), 1143–1165.

Ross, Z.E., Hauksson, E. & Ben-Zion, Y., 2017. Abundant off-fault seismicity and orthogonal structures in the San Jacinto fault zone, *Sci. Adv.,* **3**(3).

Roux, P., 2009. Passive seismic imaging with directive ambient noise: application to surface waves and the San Andreas Fault in Parkfield, CA, *Geophys. J. Int.,* **179**(1), 367–373.

Roux, P., Wathelet, M. & Roueff, A., 2011. The San Andreas Fault revisited through seismic-noise and surface-wave tomography, *Geophys. Res. Lett.,* **38**(13),.

Roux, P., Moreau, L., Lecointre, A., Hillers, G., Campillo, M., Ben-Zion, Y., Zigone, D. & Vernon, F., 2016. A methodological approach towards high-resolution surface wave imaging of the San Jacinto Fault Zone using ambient-noise recordings at a spatially dense array, *Geophys. J. Int.,* **206**(2), 980–992.

Sambridge, M., 1999. Geophysical inversion with a neighbourhood algorithm—I. Searching a parameter space, *J. Geophys. Int.,* **138**(2), 479–494.

Sanders, C.O. & Kanamori, H., 1984. A seismotectonic analysis of the Anza seismic gap, San Jacinto fault zone, southern California, *J. Geophys. Res.,* **89**(B7), 5873–5890.

Scott, J.S., Masters, T.G. & Vernon, F.L., 1994. 3-D velocity structure of the San Jacinto fault zone near Anza, California—I. *P* waves, *Geophys. J. Int.,* **119**(2), 611–626.

Shapiro, N. & Ritzwoller, M., 2002. Monte-Carlo inversion for a global shear-velocity model of the crust and upper mantle, *Geophys. J. Int.,* **151**(1), 88–105.

Shapiro, N.M., Campillo, M., Stehly, L. & Ritzwoller, M.H., 2005. High-resolution surface-wave tomography from ambient seismic noise, *Science,* **307**(5715), 1615–1618.

Tomar, G., Shapiro, N.M., Mordret, A., Singh, S.C. & Montagner, J.-P., 2016. Radial anisotropy in Valhall: ambient noise-based studies of Scholte and Love waves, *Geophys. J. Int.,* **208**(3), 1524–1539.

Tomar, G., Stutzmann, E., Mordret, A., Montagner, J.-P., Singh, S.C. & Shapiro, N.M., 2018. Joint inversion of the first overtone and fundamental mode for deep imaging at the Valhall oil field using ambient noise, *Geophys. J. Int.,* **214**(1), 122–132.

Wade, A., Arrowsmith, R., Donnellan, A., Vernon, F.L. & Ben-Zion, Y., 2017. Decameter-scale geologic structure validation of shallow seismic properties along the San Jacinto fault at Sage Brush Flat, Anza, California, in *Poster Presentation at 2017 SCEC Annual Meeting,* Los Angeles, CA.

Wathelet, M., Jongmans, D. & Ohrnberger, M., 2004. Surface-wave inversion using a direct search algorithm and its application to ambient vibration measurements, *Near Surf. Geophys.,* **2**(4), 211–221.

Xu, S. & Ben-Zion, Y., 2017. Theoretical constraints on dynamic pulverization of fault zone rocks, *Geophys. J. Int.,* **209**(1), 282–296.

Zhang, H., Maceira, M., Roux, P. & Thurber, C., 2014. Joint inversion of body-wave arrival times and surface-wave dispersion for three-dimensional seismic structure around SAFOD, *Pure Appl. Geophys.,* **171**(11), 3013–3022.

Zigone, D., Ben-Zion, Y., Campillo, M. & Roux, P., 2015. Seismic tomography of the Southern California plate boundary region from noise-based Rayleigh and Love waves, *Pure Appl. Geophys.,* **172**(5), 1007–1032.

SUPPORTING INFORMATION

Supplementary data are available at *GJI* online.

Figure S1. (Top panels) Phase and (bottom panels) group velocity depth sensitivity kernels computed at three different periods in the average velocity model for V_s, V_p and density.

Figure S2. Local depth inversion at the two locations (point A, top panel in blue and point B, bottom panel in red) in the model shown in Fig. 3, using only the group velocity dispersion curves. The inverted data are in black with the error bars; the best model and the dispersion curves associated with the best model are in grey and the colour of the modelled dispersion curves and their associated models indicate their misfit value. Note the strong non-uniqueness of the solutions with two families of models competing.

Figure S3. (Top panels) Horizontal slices in the 3-D V_p/V_s ratio model at 70 and 200 m depth. (Bottom panels) Vertical profiles. The locations of the profiles are shown in the top panels.

Please note: Oxford University Press is not responsible for the content or functionality of any supporting materials supplied by the authors. Any queries (other than missing material) should be directed to the corresponding author for the article.